Generic coexistence of Fermi arcs and Dirac cones on the surface of time-reversal invariant Weyl semimetals

Alexander Lau,[1] Jeroen van den Brink,[1,2] and Carmine Ortix[1,3]

[1] *Institute for Theoretical Solid State Physics, IFW Dresden, 01171 Dresden, Germany*
[2] *Institute for Theoretical Physics, TU Dresden, 01069 Dresden, Germany*
[3] *Institute for Theoretical Physics, Center for Extreme Matter and Emergent Phenomena, Utrecht University, Princetonplein 5, 3584 CC Utrecht, Netherlands*

(Dated: January 9, 2017)

The hallmark of Weyl semimetals is the existence of open constant-energy contours on their surface – the so-called Fermi arcs – connecting Weyl points. Here, we show that for time-reversal symmetric realizations of Weyl semimetals these Fermi arcs generically coexist with closed Fermi pockets originating from surface Dirac cones pinned to time-reversal invariant momenta. The existence of Fermi pockets is required for certain Fermi-arc connectivities due to additional restrictions imposed by the six $\mathbb{Z}_2$ topological invariants characterizing a generic time-reversal invariant Weyl semimetal. We show that a change of the Fermi-arc connectivity generally leads to a different topology of the surface Fermi surface, which is regulated by a Lifshitz transition. We further identify universal features of this coexistence in quasi-particle interference spectra that are experimentally accessible by scanning-tunneling spectroscopy.

Introduction – Sparked by the discovery of the quantum Hall effect and its theoretical explanation [1–3], the study of topological phases of matter has been one of the driving forces in modern condensed matter physics [4–9]. Novel states of matter that emerged from these investigations are, for instance, time-reversal invariant (TRI) topological insulators [10–15] or crystalline topological insulators [16–19] which are realized in several material systems.

In recent years, the family of topological materials has been extended by topological semimetals [7]. A milestone was the experimental discovery of Weyl semimetals (WSMs) [20–23]. WSMs are three-dimensional gapless materials whose bulk energy bands cross linearly at isolated points in the Brillouin zone (BZ) [24–27]. Around these so-called Weyl nodes, the system can be effectively described by a two-component Weyl Hamiltonian of the general form $H(\mathbf{k}) = \sum_{ij} k_i A_{ij} \sigma_j$, where $i = x, y, z$, and σ_j are the usual Pauli matrices with σ_0 being the identity matrix [28].

Weyl nodes are characterized by their chirality and can only be annihilated pairwise. For this reason, they are a robust bulk feature [25, 29]: generic perturbations shift the nodes in energy and momentum space without annihilating them. Most importantly, WSMs host robust surface states commonly referred to as Fermi arcs. They form an open Fermi surface connecting the surface projections of Weyl nodes with opposite chiralities [24].

Recently, it has been theoretically proposed that 2D Dirac cones and Fermi arcs can, under certain conditions, coexist at the interface between a time-reversal broken WSM and a three-dimensional (3D) TRI topological insulator [30]. The close relation between Dirac cones and Fermi arcs is also manifest in the fact that Dirac cones can be created by fusing Weyl points in a specific manner [29].

In this Letter, we show that in *time-reversal symmetric* WSMs the coexistence of Dirac cones and Fermi arcs is actually generic. It is due to additional restrictions on the surface Fermi surface imposed by the $\mathbb{Z}_2$ invariants associated with the TRI planes of the WSM. Moreover, we determine universal features of this coexistence in quasiparticle-interference (QPI) spectra, which are relevant for scanning tunneling experiments [31–35]. These spectra exhibit very distinct features related to a pronounced scattering between Dirac cones and Fermi-arcs.

$\mathbb{Z}_2$ invariants in TRI Weyl semimetals – It is well known that the existence of Weyl nodes in momentum space requires either time-reversal Θ or inversion $\mathcal{I}$ symmetry breaking [25, 26, 29]. In the presence of both symmetries all energy bands are at least doubly degenerate, which requires a linear crossing to be a four-fold degenerate Dirac point. Θ or $\mathcal{I}$ symmetry-breaking perturbations split a Dirac point into two separate Weyl points of opposite chirality.

A Weyl node represents a monopole of the Berry flux $\mathcal{A}(\mathbf{k})$ in momentum space [24, 29]. Consequently, an integral of the Berry flux over a closed surface enclosing the Weyl node results in a nonzero integer value, which defines the topological charge or chirality of the Weyl node [24, 29]. Since the total topological charge in the whole BZ must vanish [36], Weyl nodes always appear in pairs of opposite chirality. Moreover, in TRI systems each Weyl point has a time-reversal partner of same chirality, which implies the total number of Weyl nodes in these systems to be $4n$, with n being an integer [29].

The nonzero topological charge of the Weyl nodes can also be interpreted [25] as the change in the Chern number of the collection of gapped two-dimensional (2D) systems realized by decomposing the 3D BZ of a WSM in 2D momentum space cuts separating the Weyl points from each other [see Fig. 1(a)]. This property is at the basis of

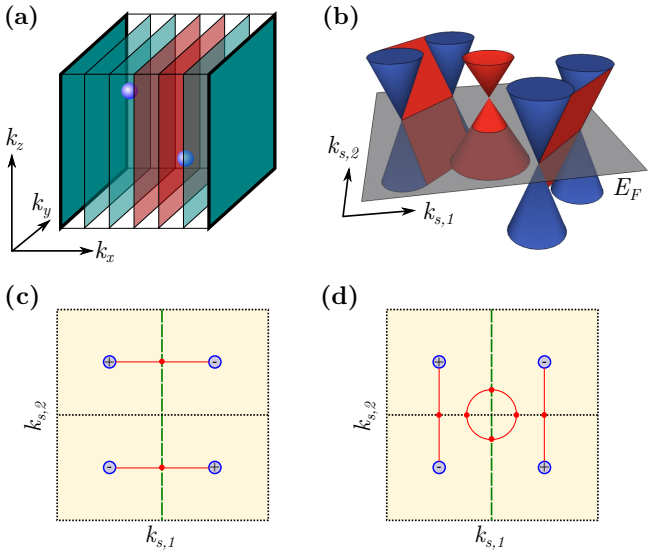

FIG. 1. (color online) (a) The BZ of a WSM can be viewed as a collection of 2D insulators with zero (green) or nonzero (red) Chern number. Weyl nodes (blue spheres) separate planes with different Chern numbers. For Θ-invariant WSMs some of the planes, indicated by bold frames, represent TRI 2D insulators that can be assigned a $\mathbb{Z}_2$ invariant. (b) Typical low-energy surface spectrum of a TRI WSM with an additional surface Dirac cone: bulk/surface states are highlighted in blue/red. (c)-(d) Fermi arc connectivities in the surface BZ of a TRI WSM with four Weyl points indicated by their topological charge ±. The surface projections of the 3D TRI planes are highlighted by dotted black ($\nu = 0$) or dashed green ($\nu = 1$) lines.

the existence of one of the most interesting hallmarks of WSMs: the existence of open constant-energy contours in the surface BZ called Fermi arcs [24].

Θ-invariant WSMs can be additionally characterized by six $\mathbb{Z}_2$ invariants, provided the Weyl points do not sit in one of the six TRI planes of the 3D BZ, which is generally the case. The Chern number of the effective 2D insulators realized by the TRI planes will be zero, but the time-reversal polarizations still allow to characterize the effective 2D systems in terms of a $\mathbb{Z}_2$ topological invariant ν [37]. Contrary to TRI insulators in 3D, where the six ν_i are not independent and can be reduced to four using homotopy arguments [38, 39] – the well-known strong and weak indices of 3D TRI insulators [11, 37] – in a Θ-invariant WSM all six $\mathbb{Z}_2$ invariants are independent and characterize the WSM as explained below.

For a generic surface of a WSM, by bulk-boundary correspondence the ν_i determine whether an even ($\nu_i = 0$) or odd ($\nu_i = 1$) number of Kramers pairs of surface states cross the Fermi level along the surface projection of the i-th TRI plane. This imposes restrictions on the structure of the surface Fermi surface but still does not uniquely determine it. Figs. 1(c) and (d) sketch two allowed but qualitatively very different surface Fermi surfaces of a Θ-invariant WSM in which the $\mathbb{Z}_2$ invariants of the planes $k_{s,2} = 0, \pi$ and $k_{s,1} = \pi$ have the trivial value 0, whereas the invariant associated with the plane at $k_{s,1} = 0$ has the nontrivial value 1. A surface Fermi surface consisting of only two open arcs, connecting Weyl points as depicted in Fig. 1(c), is entirely allowed. However, different pairs of Weyl points of opposite chirality can be connected only if an additional Fermi pocket, enclosing a time-reversal invariant point, is created [see Fig. 1(d)]. The latter situation is a unique signature of Fermi arcs coexisting with a protected surface Dirac cone [see Fig. 1(b)], which is an exclusive feature of TRI Weyl semimetals. We emphasize that while the transition between the two different Fermi-arc connectivities does not change the $\mathbb{Z}_2$ invariants of the Θ-invariant WSM, the change of the Fermi surface topology does imply a Lifshitz transition on the surface the material [40, 41]. Before studying this Lifshitz transition in an explicit Hamiltonian, we first determine the generic consequences for QPI. This we compare to explicit QPI calculations for the explicit Hamiltonian later on.

Phenomenological QPI patterns – Having established the generic coexistence of Fermi arcs and Dirac cones in Θ-invariant WSM, we now proceed to analyze their fingerprints in QPI patterns, which can be observed in scanning tunneling spectroscopy experiments [31–35]. We start out by noticing that QPI spectra can be approximated in terms of the joint density of states (JDOS) [31, 42],

$$J(\mathbf{q}, E) = \int d^2k\, A(\mathbf{k}+\mathbf{q}, E) A(\mathbf{k}, E), \qquad (1)$$

where $\mathbf{k}$ is the momentum parallel to the surface, and $A(\mathbf{k}, E) = -1/2\pi\, \mathrm{Im}\{\mathrm{Tr}[G_s(\mathbf{k}, E)]\}$ is the spectral function with the surface Green's function $G_s(\mathbf{k}, E)$.

We first illustrate the key points of the JDOS patterns phenomenologically, assuming constant nonzero curvature and constant spectral density for both Fermi arcs and Fermi pockets. The ensuing spectral functions can be written as:

$$A_i(\mathbf{k}) = \int_{\alpha_i}^{\alpha_i+\Delta\alpha_i} d\alpha' \delta(\mathbf{k} - [\mathbf{K}_i + R_i\,(\cos\alpha', \sin\alpha')]), \quad (2)$$

where i labels the Fermi arcs and the Fermi pocket. Clearly, $\Delta\alpha_{\mathrm{pocket}} = 2\pi$ for the circular Fermi pocket, while for a Fermi arc α_{arc} and $\alpha_{\mathrm{arc}} + \Delta\alpha_{\mathrm{arc}}$ determine the end points corresponding to the connected Weyl points. Fig. 2(a) shows the idealized Fermi surface for the conventional surface bandstructure of a Θ-invariant WSM with two Fermi arcs. The corresponding JDOS, shown in Fig. 2(b), displays the characteristic feature of the open Fermi surface of WSMs: the existence of a pinch point at $\mathbf{q} \equiv 0$ [32]. An additional, crescent-shaped pattern is encountered at a distance corresponding to the distance between the Fermi arcs in the BZ, and originates from scattering events between the two Fermi arcs.

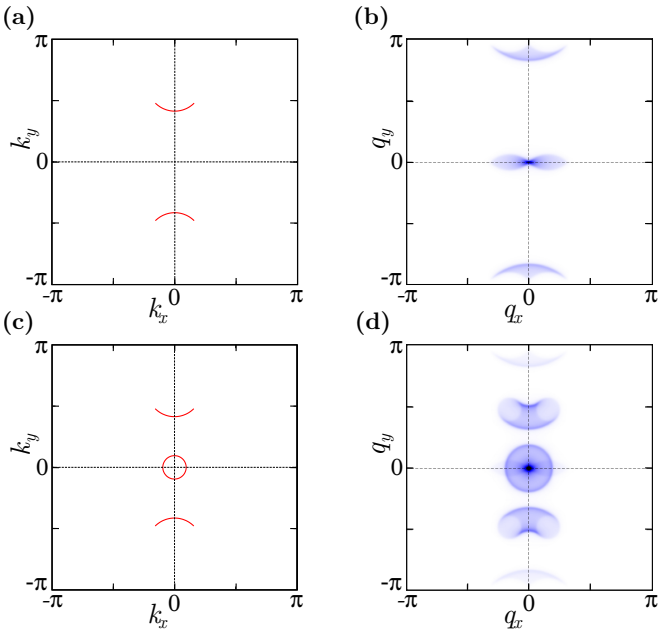

FIG. 2. (color online) Analytical consideration of the joint density of states: (a) Fermi surface consisting of two Fermi arcs only. The corresponding JDOS in (b) shows the characterisitc pinch point at $\mathbf{q} = 0$. (c) A Fermi surface with additional circular Fermi pocket shows additional features in the JDOS as shown in (d). Most remarkable are the kidney-shaped features stemming from scattering between Fermi pocket and Fermi arcs.

For a Fermi surface with an additional circular Fermi pocket, the JDOS pattern changes qualitatively [see Figs. 2(c), (d)]. First, we see that the pinch point is washed out by the presence of a disk pattern of radius $2R_{\text{pocket}}$ with a high-intensity peak at $\mathbf{q} = 0$. This feature stems from scattering events within the Fermi pocket. Second and most imporantly, we find two additional kidney-shaped patterns at a distance $|\mathbf{q}|$ corresponding to the distance between Fermi arcs and Fermi pocket that can be thus attributed to scattering events between Fermi pocket and Fermi arcs. Each of them follows the shape of the Fermi arcs with a broadening equal to the diameter of the Fermi pocket. These patterns represent the universal QPI feature of the coexistence of Fermi arcs with a Dirac cone on the surface of Θ-invariant WSMs. It should be noted that the crescent-shaped patterns are still present but of weaker intensity as compared to the QPI patterns due to the presence of the Fermi pocket.

Tight-binding model formulation – Next, we introduce a tight-binding model for a Θ-invariant WSM to investigate on a microscopic basis the coexistence of surface Dirac cones and Fermi arcs. The tight-binding model is defined on a cubic lattice and reads

$$\begin{aligned} H(\mathbf{k}) = a\,(\sin k_x\,\tau^1 s^3 + \sin k_y\,\tau^2 s^0) + \beta\,\tau^2 s^2 + d\,\tau^2 s^3 \\ + [t\cos k_z + 2b(2 - \cos k_x - \cos k_y)]\,\tau^3 s^0 \\ + \alpha \sin k_y\,\tau^1 s^2 + \lambda \sin k_z\,\tau^0 s^1, \end{aligned} \tag{3}$$

where the s^i are Pauli matrices in spin space, whereas the τ^i are Pauli matrices associated with additional orbital degrees of freedom. The lattice constant has been set to unity. The Hamiltonian is based on the perhaps simplest and most elementary tight-binding model that describes a TRI WSM, introduced in Ref. 32.

The model preserves time-reversal symmetry with $\Theta = i\tau^0 s^2\,K$, $\mathbf{k} \to -\mathbf{k}$, where K is complex conjugation. The β, d and λ terms break inversion symmetry with the inversion operator $P = \tau^3 s^0$, $\mathbf{k} \to -\mathbf{k}$, which is a necessary condition for the existence of a Weyl semimetal phase.

In the following we will analyze $H(\mathbf{k})$ in a finite geometry. For the analysis of the energy spectrum, we choose the system to have open boundary conditions in the y direction and periodic boundary conditions in the x and z direction. This gives rise to two (010) surfaces. The energies of the system are then obtained from exact numerical diagonalization of the corresponding tight-binding Hamiltonian in mixed position-momentum space associated with Eq. (3). The topological charge of the bulk Weyl nodes is obtained from the bulk Hamiltonian by integration of the Berry flux over the surface of a BZ volume containing the Weyl node. The $\mathbb{Z}_2$ invariants ν_i of the time-reversal invariant planes are instead computed using a Wannier-center formulation of the topological invariant (see Refs. 43 and 44). Furthermore, we will compute the JDOS corresponding to the (010) surface of a semi-infinite slab of the system described by Eq. (3). For that, we determine the (010) surface Green's function of the system using an iterative scheme (see Refs. 43 and 45). In all calculations we assume the Fermi energy to be at $E_F = 0$.

To demonstrate the coexistence of surface Dirac cones and Fermi arcs in $H(\mathbf{k})$, we start from a particular Weyl semimetal phase and vary the parameter β. The results are presented in Fig. 3. With the chosen parameters, the model features four bulk Weyl points of charge ± 1 which are all located away from the time-reversal invariant planes of the bulk BZ. Hence, all six $\mathbb{Z}_2$ invariants are well-defined. In particular, we find that $\nu_{k_z=\pi} = 1$ while the remaining five $\mathbb{Z}_2$ invariants are zero. At the (010) surface we therefore expect an odd number of Kramers pairs at $k_z = \pi$ and an even number of Kramers pairs at $k_z = 0$ and $k_x = 0, \pi$. Furthermore, the surface projections of the four Weyl nodes appear in different quadrants of the surface BZ.

For large values of β, we find that Fermi arcs connect two Weyl nodes in the left half-plane and two Weyl nodes in the right half-plane [see Fig. 3(a)]. The fact that the Fermi arcs cross only the line $k_z = \pi$ is in agreement

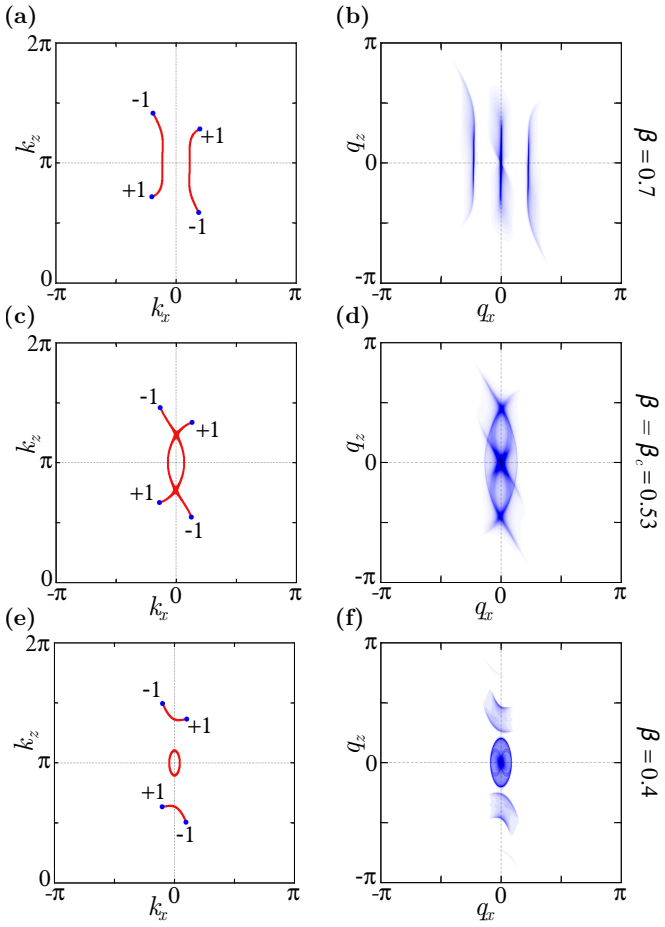

FIG. 3. (color online) Fermi surfaces and JDOS for (010) surfaces in the tight-binding model with $a = b = 1$, $t = 1.5$, $\alpha = 0.3$, $d = 0.1$, $\lambda = 0.5$, and $E_F = 0$: the first row shows the Fermi surfaces for different values of the parameter β. The bulk Weyl nodes are highlighted in blue and their topological charge is indicated. Surface states are highlighted in red. The second row shows the corresponding JDOS spectra. In (f), the kidney-shaped features indicative of the coexistence of Fermi arcs and Dirac cones are clearly visible in the JDOS. Also note how the Fermi-surface topology changes with β while passing a surface Lifshitz transition at $\beta = \beta_c \approx 0.53$.

with the values of the topological invariants. In Fig. 3(b) we show the corresponding JDOS. We see an elongated "figure-eight" feature aligned with the q_z axis and two crescent-shaped patterns parallel to it, which occur at $\mathbf{q}$ values corresponding to the mutual distance of the Fermi arcs in the surface BZ.

By decreasing the parameter β, the Fermi arcs are bent towards each other until they intersect at a critical value of β [see Fig. 3(c)]. This point corresponds to the Lifshitz transition at which the connectivity of the Fermi arcs changes. Note that the position of the Weyl nodes has barely changed. A further decrease in the parameter β reveals the coexistence of Dirac cones and Fermi arcs [see Fig. 3(e)]: surface Fermi arcs connect two Weyl nodes in the upper half-plane and two Weyl nodes in the lower half-plane of the surface BZ. In addition to the open-arc features, we find an elliptical Fermi pocket of surface states around the $\bar{Z}$ point of the surface BZ. The existence of the Fermi pocket is required for this particular connectivity of Weyl nodes to satisfy the number of surface states imposed by the topological invariants ν_i which have not changed during the Lifshitz transition. From an analysis of the surface band structure [43], we find that the Fermi pocket originates from a *dangling* surface Dirac cone. This type of Dirac cone connects bulk conduction to bulk valence bands not along all directions of the surface BZ, as would be the case for a 3D topological insulator. This is only possible in TRI Weyl semimetals due to the lack of a global relation between the $\mathbb{Z}_2$ invariants.

The JDOS of this configuration is in perfect agreement with the analytical considerations above [see Fig. 3(f)]: we find the elliptical inter-pocket feature with a pronounced central peak around the origin, whose semi-axes are twice as large as those of the associated Fermi pocket in the surface BZ. We do not clearly see a characteristic intra-arc feature, most likely because its intensity is too weak as compared to the Fermi pocket features. Also the inter-arc features are barely visible due to the small size of the Fermi arcs and, concomitantly, the small phase-space volume for scattering between them. However, their position and shape agree with the expectation from our simple analytical consideration. Most importantly, we find the kidney-shaped features indicative of scattering between the Fermi arcs and the Fermi pocket. As expected, the broadening equals the size of the Fermi pocket whereas their position corresponds to the distance between Fermi pocket and Fermi arcs. The comparison of Figs. 3(b) and (f) shows that the different Fermi arc connectivities are reflected in distinct universal JDOS features.

Conclusions – Besides the topological charges of the Weyl nodes, a generic TRI Weyl semimetal can be characterized by six $\mathbb{Z}_2$ invariants associated with the TRI planes of the 3D BZ. In contrast to a fully gapped system with time-reversal symmetry, these invariants are all independent. For the surface of a TRI WSM, they impose restrictions on the number of surface Kramers pairs along the surface projections of the TRI planes and, therefore, also on the structure of the Fermi arcs which connect the Weyl nodes on the surface. Nevertheless, a remaining modulo-two ambiguity gives rise to many possible and qualitatively different Fermi-arc connectivities. In particular, certain connectivities require the creation of a Fermi pocket which is connected to the presence of a surface Dirac cone pinned to a TRI momentum. This changes the topology of the Fermi surface and is, thus, accompanied by a Lifshitz transition. It is crucial to note that this transition does not change the $\mathbb{Z}_2$ invariants and is, therefore, generic to all TRI Weyl semimetals. We have further shown that the coexistence

of Fermi arcs and Dirac cones leads to universal, kidney-shaped features in the QPI patterns. This result suggests that there can be unambiguous signatures for the coexistence of Fermi arcs and Dirac cones in scanning tunneling spectroscopy experiments.

We acknowledge the financial support of the Future and Emerging Technologies (FET) programme within the Seventh Framework Programme for Research of the European Commission under FET-Open grant number: 618083 (CNTQC). This work has been supported by the Deutsche Forschungsgemeinschaft under Grant No. OR 404/1-1 and SFB 1143.

[1] K. v. Klitzing, G. Dorda, and M. Pepper, Phys. Rev. Lett. **45**, 494 (1980).
[2] D. J. Thouless, M. Kohmoto, M. P. Nightingale, and M. den Nijs, Phys. Rev. Lett. **49**, 405 (1982).
[3] M. Kohmoto, Ann. Phys. **160**, 343 (1985).
[4] X.-L. Qi and S.-C. Zhang, Rev. Mod. Phys. **83**, 1057 (2011).
[5] M. Z. Hasan and C. L. Kane, Rev. Mod. Phys. **82**, 3045 (2010).
[6] M. Sato and Y. Ando, ArXiv e-prints (2016), arXiv:1608.03395 [cond-mat.supr-con].
[7] A. A. Burkov, Nat. Mater. **15**, 1145 (2016).
[8] T. Senthil, Annu. Rev. Condens. Matter Phys. **6**, 299 (2015).
[9] A. Lau, C. Ortix, and J. van den Brink, Phys. Rev. Lett. **115**, 216805 (2015).
[10] C. L. Kane and E. J. Mele, Phys. Rev. Lett. **95**, 226801 (2005).
[11] L. Fu, C. L. Kane, and E. J. Mele, Phys. Rev. Lett. **98**, 106803 (2007).
[12] B. A. Bernevig, T. L. Hughes, and S.-C. Zhang, Science **314**, 1757 (2006).
[13] M. König, S. Wiedmann, C. Brüne, A. Roth, H. Buhmann, L. W. Molenkamp, X.-L. Qi, and S.-C. Zhang, Science **318**, 766 (2007).
[14] Y. Xia, D. Qian, D. Hsieh, L. Wray, A. Pal, H. Lin, A. Bansil, D. Grauer, Y. S. Hor, R. J. Cava, and M. Z. Hasan, Nat. Phys. **5**, 398 (2009).
[15] C. Pauly, B. Rasche, K. Koepernik, M. Liebmann, M. Pratzer, M. Richter, J. Kellner, M. Eschbach, B. Kaufmann, L. Plucinski, C. M. Schneider, M. Ruck, J. van den Brink, and M. Morgenstern, Nat. Phys. **11**, 338 (2015).
[16] Y. Ando and L. Fu, Annu. Rev. Condens. Matter Phys. **6**, 361 (2015).
[17] L. Fu, Phys. Rev. Lett. **106**, 106802 (2011).
[18] Y. Tanaka, Z. Ren, T. Sato, K. Nakayama, S. Souma, T. Takahashi, K. Segawa, and Y. Ando, Nat. Phys. **8**, 800 (2012).
[19] A. Lau, J. van den Brink, and C. Ortix, Phys. Rev. B **94**, 165164 (2016).
[20] S.-M. Huang, S.-Y. Xu, I. Belopolski, C.-C. Lee, G. Chang, B. Wang, N. Alidoust, G. Bian, M. Neupane, C. Zhang, S. Jia, A. Bansil, H. Lin, and M. Z. Hasan, Nat. Commun. **6**, 7373 (2015).
[21] B. Q. Lv, H. M. Weng, B. B. Fu, X. P. Wang, H. Miao, J. Ma, P. Richard, X. C. Huang, L. X. Zhao, G. F. Chen, Z. Fang, X. Dai, T. Qian, and H. Ding, Phys. Rev. X **5**, 031013 (2015).
[22] S.-Y. Xu, I. Belopolski, N. Alidoust, M. Neupane, G. Bian, C. Zhang, R. Sankar, G. Chang, Z. Yuan, C.-C. Lee, S.-M. Huang, H. Zheng, J. Ma, D. S. Sanchez, B. Wang, A. Bansil, F. Chou, P. P. Shibayev, H. Lin, S. Jia, and M. Z. Hasan, Science **349**, 613 (2015).
[23] E. Haubold, K. Koepernik, D. Efremov, S. Khim, A. Fedorov, Y. Kushnirenko, J. van den Brink, S. Wurmehl, B. Buchner, T. K. Kim, M. Hoesch, K. Sumida, K. Taguchi, T. Yoshikawa, A. Kimura, T. Okuda, and S. V. Borisenko, ArXiv e-prints (2016), arXiv:1609.09549 [cond-mat.mes-hall].
[24] X. Wan, A. M. Turner, A. Vishwanath, and S. Y. Savrasov, Phys. Rev. B **83**, 205101 (2011).
[25] A. A. Burkov and L. Balents, Phys. Rev. Lett. **107**, 127205 (2011).
[26] A. A. Zyuzin, S. Wu, and A. A. Burkov, Phys. Rev. B **85**, 165110 (2012).
[27] T. Ojanen, Phys. Rev. B **87**, 245112 (2013).
[28] A. A. Soluyanov, D. Gresch, Z. Wang, Q. Wu, M. Troyer, X. Dai, and B. A. Bernevig, Nature **527**, 495 (2015).
[29] R. Okugawa and S. Murakami, Phys. Rev. B **89**, 235315 (2014).
[30] A. G. Grushin, J. W. F. Venderbos, and J. H. Bardarson, Phys. Rev. B **91**, 121109 (2015).
[31] P. G. Derry, A. K. Mitchell, and D. E. Logan, Phys. Rev. B **92**, 035126 (2015).
[32] S. Kourtis, J. Li, Z. Wang, A. Yazdani, and B. A. Bernevig, Phys. Rev. B **93**, 041109 (2016).
[33] G. Chang, S.-Y. Xu, H. Zheng, C.-C. Lee, S.-M. Huang, I. Belopolski, D. S. Sanchez, G. Bian, N. Alidoust, T.-R. Chang, C.-H. Hsu, H.-T. Jeng, A. Bansil, H. Lin, and M. Z. Hasan, Phys. Rev. Lett. **116**, 066601 (2016).
[34] R. Batabyal, N. Morali, N. Avraham, Y. Sun, M. Schmidt, C. Felser, A. Stern, B. Yan, and H. Beidenkopf, Science Advances **2**, e1600709 (2016).
[35] H. Zheng, S.-Y. Xu, G. Bian, C. Guo, G. Chang, D. S. Sanchez, I. Belopolski, C.-C. Lee, S.-M. Huang, X. Zhang, R. Sankar, N. Alidoust, T.-R. Chang, F. Wu, T. Neupert, F. Chou, H.-T. Jeng, N. Yao, A. Bansil, S. Jia, H. Lin, and M. Z. Hasan, ACS Nano **10**, 1378 (2016).
[36] H. Nielsen and M. Ninomiya, Nuclear Physics B **193**, 173 (1981).
[37] L. Fu and C. L. Kane, Phys. Rev. B **74**, 195312 (2006).
[38] J. E. Moore and L. Balents, Phys. Rev. B **75**, 121306 (2007).
[39] R. Roy, Phys. Rev. B **79**, 195322 (2009).
[40] G. E. Volovik, ArXiv e-prints (2016), arXiv:1606.08318 [cond-mat.other].
[41] A. Varlet, M. Mucha-Kruczyński, D. Bischoff, P. Simonet, T. Taniguchi, K. Watanabe, V. Fal'ko, T. Ihn, and K. Ensslin, ArXiv e-prints (2015), arXiv:1508.02922 [cond-mat.mes-hall].
[42] L. Simon, F. Vonau, and D. Aubel, Journal of Physics: Condensed Matter **19**, 355009 (2007).
[43] See Supplemental Material at [url] for a detailed analytical treatment of the JDOS, for the Wannier-center method used for the calculation of $\mathbb{Z}_2$ invariants, for the iterative scheme used for the calculation of surface Green's functions, and for a discussion of the surface spectra of the tight-binding model.
[44] R. Yu, X. L. Qi, A. Bernevig, Z. Fang, and X. Dai, Phys. Rev. B **84**, 075119 (2011).

[45] M. P. L. Sancho, J. M. L. Sancho, and J. Rubio, Journal of Physics F: Metal Physics **15**, 851 (1985).

SUPPLEMENTAL MATERIAL

A: Analytical treatment of the JDOS

In scanning-tunneling spectroscopy (STS) experiments, the differential conductance between the tip and the surface of a material is used to obtain a spatial map of the local density of electronic states (LDOS) at a certain energy and temperature [1, 2]. Impurities lead to characteristic modulations in the LDOS that depend strongly on the electronic structure of the host material and on the properties and distribution of impurities. In particular, impurities break translational symmetry on the surface thereby enabling scattering between states with the same energy $E = E_F$ but different momentum $\mathbf{k}$ and $\mathbf{k}'$. The modulations in the LDOS can be analyzed with Fourier-transform STS (FT-STS). In this way, the Fourier transformed LDOS (FTLDOS) is interpreted in terms of the quasiparticle interference (QPI) between diagonal states of the clean host material [1, 2].

Typically, the FTLDOS is approximated by the joint density of states (JDOS) [31, 42], which is expressed as

$$J(\mathbf{q}, E) = \int d^2k\, A(\mathbf{k}+\mathbf{q}, E) A(\mathbf{k}, E), \tag{4}$$

$$A(\mathbf{k}, E) = -1/2\pi\, \mathrm{Im}\{\mathrm{Tr}[G_s(\mathbf{k}, E)]\}, \tag{5}$$

where $A(\mathbf{k}, E)$ is the spectral function, $G_s(\mathbf{k}, E)$ is the surface Green's function, and $\mathbf{k}$ is the momentum parallel to the surface.

In order to obtain a phenomenological picture of the QPI patterns on the surface of Weyl semimetals, we consider an idealized Fermi surface consisting of a circular Fermi pocket around the origin which is surrounded by an open Fermi arc of constant curvature and its time-reversal partner [see Fig. 2(c) in the main text]. Furthermore, we assume constant spectral density. The spectral function of the system can then be decomposed as $A = A_p + A_{a_1} + A_{a_2}$ with

$$A_p(\mathbf{k}) = \int_0^{2\pi} d\alpha'\, \delta(\mathbf{k} - R_p\,(\cos\alpha', \sin\alpha')]), \tag{6}$$

$$A_{a_{1,2}}(\mathbf{k}) = \int_\alpha^{\alpha+\Delta\alpha} d\alpha'\, \delta(\mathbf{k} \mp [\mathbf{K} + R_a\,(\cos\alpha', \sin\alpha')]). \tag{7}$$

A_p is the spectral function associated with the circular Fermi pocket of radius R_p. $A_{a_{1,2}}$ are the contributions from the two Fermi arcs. The arcs are cut out from circles centered at $\pm\mathbf{K}$ with radius R_a. The end points of the arcs are at $\pm\alpha$ and $\pm\alpha \pm \Delta\alpha$. With this decomposition, the JDOS of Eq. (4) becomes

$$\begin{aligned} J(\mathbf{q}) = \int d^2k\, [&\underbrace{A_{a_1}(\mathbf{k}+\mathbf{q})A_{a_1}(\mathbf{k}) + A_{a_2}(\mathbf{k}+\mathbf{q})A_{a_2}(\mathbf{k})}_{\text{intra-arc}} \\ &+ \underbrace{A_{a_1}(\mathbf{k}+\mathbf{q})A_{a_2}(\mathbf{k}) + A_{a_2}(\mathbf{k}+\mathbf{q})A_{a_1}(\mathbf{k})}_{\text{inter-arc}} \\ &+ \underbrace{A_p(\mathbf{k}+\mathbf{q})[A_{a_1}(\mathbf{k}) + A_{a_2}(\mathbf{k})]}_{\text{arc-pocket}} \\ &+ \underbrace{[A_{a_1}(\mathbf{k}+\mathbf{q}) + A_{a_2}(\mathbf{k}+\mathbf{q})]A_p(\mathbf{k})}_{\text{arc-pocket}} \\ &+ \underbrace{A_p(\mathbf{k}+\mathbf{q})A_p(\mathbf{k})}_{\text{intra-pocket}}]. \end{aligned} \tag{8}$$

We see that there are four different contributions to the total JDOS which can be attributed to scattering events within each Fermi arc (intra-arc), between the Fermi arcs (inter-arc), between Fermi pocket and Fermi arcs (arc-pocket), and within the Fermi pocket (intra-pocket). Inserting Eqs. (6) and (7), each individual contribution involves integrals of the form

$$\int d^2k \int d\alpha'\, d\alpha''\, \delta[\mathbf{k} + \mathbf{q} - \mathbf{u}_i(\alpha')]\, \delta[\mathbf{k} - \mathbf{u}_j(\alpha'')]. \tag{9}$$

This can be written as a convolution of two δ functions, $\delta * \delta$. By using that $\delta * \delta \equiv \delta$, the integral becomes

$$\int d\alpha'\, d\alpha''\, \delta[\mathbf{q} + \mathbf{u}_i(\alpha')]\, \delta[\mathbf{u}_j(\alpha'')]. \tag{10}$$

In general, this integral cannot be simplified further. To obtain qualitative results for the JDOS, we therefore approximate the appearing δ functions of the form $\delta(\mathbf{k}) \equiv \delta(k_x)\delta(k_y)$ by Lorentz functions

$$\delta_\epsilon(k_i) = \frac{1}{\pi}\, \frac{\epsilon}{k_i^2 + \epsilon^2}, \quad \epsilon \ll 1, \tag{11}$$

with height $1/\sqrt{\epsilon}$ and width $\sqrt{\epsilon}$. The ensuing integrals are then solved numerically. The results for the different JDOS contributions are shown in Fig. 4. Note that in each panel the color scale is renormalized with respect to the considered contribution.

Fig. 4(a) shows the intra-arc JDOS contributions. We can clearly see a pinch point at $\mathbf{q} = 0$ which is in the center of a dumbell-shaped feature aligned with the q_x axis. This is the unique QPI pattern of an open Fermi arc. Since the considered Fermi surface consists of two of those arcs, we get an additional JDOS (inter-arc) contribution originating from scattering between the arcs. These features appear around the q_y axis at $\mathbf{q}$ vectors corresponding to scattering vectors between the two arcs in the BZ [see Fig. 4(b)].

The intra-cone JDOS contribution, shown in Fig. 4(c), is strongly peaked at $\mathbf{q} = 0$ and falls off rapidly away from the center. The resulting pattern is rotationally symmetric reflecting the symmetry of the Fermi pocket. The

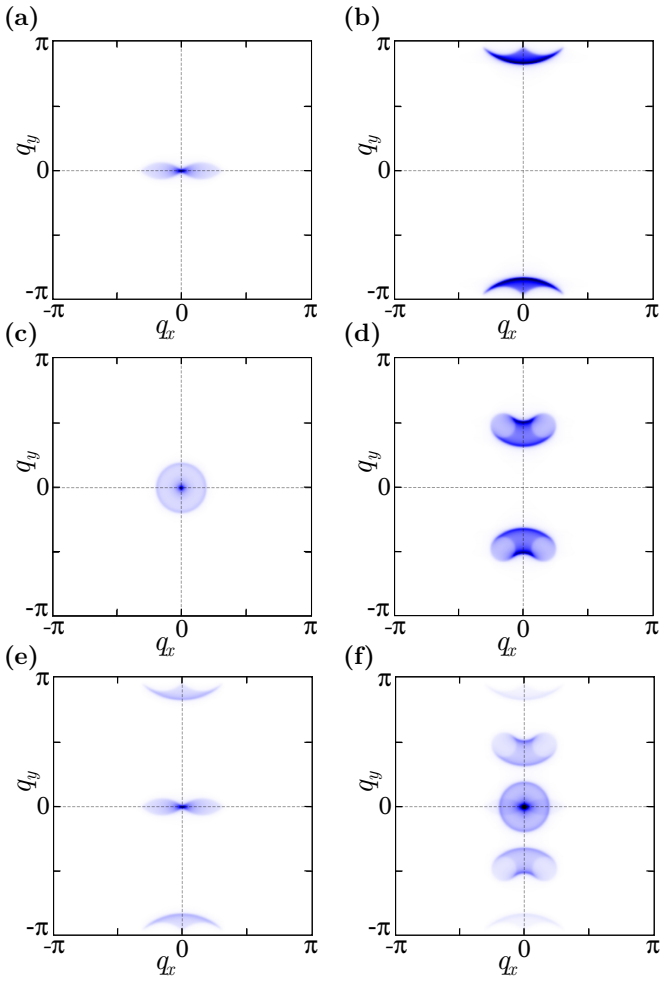

FIG. 4. (color online) JDOS contributions from an analytical treatment: (a) intra-arc scattering, (b) inter-arc scattering, (c) intra-pocket scattering, (d) arc-pocket scattering. Note that in each panel the color scale is renormalized with respect to the considered JDOS contribution. The color scale ranges from white (small JDOS), over blue to black (high JDOS). We also show the accumulated JDOS corresponding to Fermi surfaces with: (e) two Fermi arcs only, (f) two Fermi arcs and an additional Fermi pocket in the center.

feature has a sharp boundary with a slightly enhanced intensity at $|\mathbf{q}|$ values corresponding to the diameter of the underlying Fermi pocket. This is due to scattering events from opposing states of the Fermi pocket.

In Fig. 4(d) we present the arc-pocket JDOS contribution which is characteristic of the coexistence of open Fermi arcs and closed Fermi pockets. It therefore represents the universal QPI pattern of Weyl semimetals with additional surface Dirac cones. The kidney-shaped features appear around the q_y axis at $\mathbf{q}$ vectors corresponding to scattering vectors that connect the open Fermi arcs to the closed Fermi pocket.

All separate JDOS contributions presented in Figs. 4(a)-(d) have very different intensities. This can be accounted for by the phase-space volume available for scattering events contributing to the considered JDOS contribution. Accordingly, the intra-pocket features are very high in intensity whereas the inter-arc contributions are very low. This is most apparent in the accumulated JDOS spectra which we show in Figs. 4(e) and (f).

In Fig. 4(e), we show the accumulated JDOS taking into account only intra- and inter-arc contributions, which corresponds to a Fermi surface consisting only of two open Fermi arcs [see Fig. 2(a) in the main text]. On the contrary, in Fig. 4(f) we accumulate all four JDOS contributions. We can clearly see how the total JDOS is dominated by QPI features stemming from scattering events involving the Fermi pocket.

B: Wannier-center formulation of the $\mathbb{Z}_2$ invariant

In the following, we are going to review a method, introduced in Ref. 3, that enables us to calculate the topological $\mathbb{Z}_2$ invariant of a general 2D insulator with time-reversal symmetry. This method allows us to calculate the $\mathbb{Z}_2$ number without choosing a gauge-fixing condition, which makes it particularly appealing for numerical studies.

The central notion of this method is the *time-reversal polarization* [4]. In a time-reversal invariant 1D band insulator, the $2N$ occupied bands can be decomposed into two sets which are connected by time reversal. The time-reversal polarization is then the difference in the net charge polarization of the two sets of bands. Furthermore, it can be shown that the time-reversal polarization can only assume the values 0 or 1 (modulo 2) as long as the system preserves time-reversal symmetry.

A 2D time-reversal invariant (TRI) band insulator can be thought of as a collection of 1D insulators in momentum space parametrized by, say, k_y. In this collection, only the effective 1D systems at $k_y = 0$ and π preserve 1D time-reversal symmetry. Thus, the time-reversal polarization can assume non-integer values in between. The key idea is now to determine how the time-reversal polarization changes with k_y. It was shown that this leads to a well-defined $\mathbb{Z}_2$ invariant for a 2D band insulator [3, 4]. Moreover, the charge polarization of an occupied band is related to its Wannier center in position space. For this reason, the change in time-reversal polarization can also be understood as a shift of the Wannier centers.

The Wannier centers of the occupied bands at fixed k_y are defined as the eigenvalues of the position operator projected onto the occupied subspace. By using localized Wannier functions $|\alpha j\rangle$ as a basis, where α is an orbital index and j denotes the lattice site, the position operator for a 1D lattice system with periodic boundary conditions can be written as

$$\hat{X} = \sum_{\alpha j} e^{-i\frac{2\pi j}{N_x}} |\alpha j\rangle\langle\alpha j|, \tag{12}$$

where N_x is the number of unit cells. Furthermore, the projection operator onto the occupied bands o at fixed k_y is defined as

$$\hat{P}(k_y) = \sum_{n\in o, k_x} |\Psi_{nk_xk_y}\rangle\langle\Psi_{nk_xk_y}|, \tag{13}$$

with the Bloch state $|\Psi_{n\mathbf{k}}\rangle = e^{i\mathbf{k}\cdot\mathbf{r}}|n\mathbf{k}\rangle$. The projected position operator can be written as follows

$$\begin{aligned}\hat{X}_P(k_y) &= \hat{P}(k_y)\hat{X}\hat{P}(k_y) \\ &= \sum_{j=1}^{N_x}\sum_{mn\in o} |\Psi_{n,k_{x,j},k_y}\rangle\langle\Psi_{n,k_{x,j+1},k_y}|F^{nm}_{j,j+1}(k_y),\end{aligned} \tag{14}$$

with $k_{x,j} = 2\pi j/N_x$ being the discrete k_x points taken along the x axis. The $F_{j,j+1}(k_y)$ are $2N\times 2N$ matrices with matrix elements

$$F^{nm}_{j,j+1}(k_y) = \langle n, k_{x,j}, k_y|m, k_{x,j+1}, k_y\rangle. \tag{15}$$

The eigenvalues of $\hat{X}_P(k_y)$ can be obtained by the transfer matrix method. For this purpose, we define the $2N\times 2N$ matrix

$$T(k_y) = F_{1,2}F_{2,3}\cdots F_{N_x-1,N_x}F_{N_x,1}. \tag{16}$$

T is unitary and has the following eigenvalues

$$\lambda_m(k_y) = e^{i\theta_m(k_y)}, \quad m = 1, 2, \ldots, 2N, \tag{17}$$

which are gauge invariant under $U(2N)$ transformations of the $|n\mathbf{k}\rangle$. Furthermore, it can be shown that in the continuum limit $T(k_y)$ corresponds to the $U(2N)$ Wilson loop [44],

$$T(k_y) = P\, e^{-i\int_{C_{k_y}} A(k_x)\, dk_x}, \tag{18}$$

with the non-Abelian Berry connection $A(k)$ which is a unitary $2N\times 2N$ matrix. The eigenvalues of the projected position operator $\hat{X}_P(k_y)$, and thus the Wannier centers of the occupied bands, are then obtained from the eigenvalues of T as

$$\chi_{m,j}(k_y) = e^{i[\theta_m(k_y)+2\pi j]/N_x}, \quad j = 1, \ldots N_x. \tag{19}$$

Since the Wannier centers of adjacent unit cells differ only by a constant, k_y independent phase shift $e^{i2\pi/N_x}$, it is sufficient to look at the evolution of the $2N$ phases $\theta_m(k_y) = \mathrm{Im}\,\log\lambda_m(k_y)$.

The connection to the $\mathbb{Z}_2$ invariant is established as follows. We plot the $2N$ phases θ_m as a function of k_y and glue the lines $\theta = -\pi$ and $\theta = \pi$ together, such that the Wannier centers live on the surface of a cylinder. At $k_y = 0$ the phases have to appear as degenerate pairs due to time-reversal symmetry. By moving away from this point, the pairs split and recombine at $k_y = \pi$ (again due to time-reversal symmetry). Because the θ_m are phases, the Wannier center pairs may now differ by an integer multiple of 2π. Hence, the evolution of the Wannier center pairs from $k_y = 0$ to $k_y = \pi$ will encircle the cylinder an integer number of times. The sum of these integers over all pairs of Wannier centers defines a winding number. However, an even number of windings can always be removed, whereas this is not possible for a single winding. Consequently, the total winding number modulo 2 is a topological $\mathbb{Z}_2$ invariant.

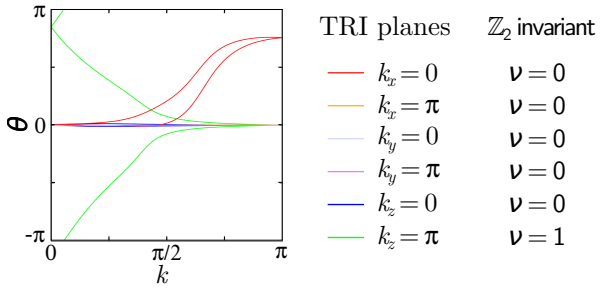

FIG. 5. (color online) Evolution of the Wannier centers θ_m as a function of k for the TRI planes of the tight-binding model with $a = b = 1$, $t = 1.5$, $\alpha = 0.3$, $d = 0.1$, $\lambda = 0.5$ and $\beta = 0.7$. k denotes a momentum parallel to the considered plane in the 3D BZ. We also indicate the corresponding value of the $\mathbb{Z}_2$ invariant ν inferred from the winding number of the Wannier pair.

As an example, in Fig. 5 we show the evolution of the θ_m for the six TRI planes of the tight-binding model considered in the main text. There are only two occupied bands which is why we only need to look at a single pair of Wannier centers for each plane. We find that only the Wannier pair for the TRI plane at $k_z = \pi$ winds nontrivially around the θ-k cylinder. Hence, we infer that the $\mathbb{Z}_2$ invariant of this plane is $\nu = 1$. All other TRI planes have a trivial $\mathbb{Z}_2$ number, i.e., $\nu = 0$.

C: Iterative scheme for the calculation of the surface Green's function

In order to calculate the surface JDOS of a lattice system, we need to compute its corresponding surface Green's function. In the following, we are going to review an iterative scheme, introduced in Ref. 5, for the computation of this surface Green's function. For simplicity, we will restrict our considerations to systems described by tight-binding Hamiltonians with only nearest-neighbor hopping terms. We note, however, that any solid with a surface can be reduced to a semi-infinite stack of principal layers with nearest-neighbor interactions [5].

Let us consider a tight-binding model described by the lattice Hamiltonian $\mathcal{H}$. A surface can be introduced by cleaving the lattice along a principal layer of unit cells. Each unit cell in this layer may have M degrees of freedom, such as spin, orbital or sublattice degrees of free-

dom. Let us further assume that the system preserves translational symmetry parallel to the surface. Consequently, the momentum $\mathbf{k}_{||}$ parallel to the surface is a good quantum number and we can form Bloch-state vectors for each principal layer of the form

$$\Psi_n(\mathbf{k}_{||}) = (\varphi_n^1(\mathbf{k}_{||}), \ldots, \varphi_n^M(\mathbf{k}_{||})), \tag{20}$$

where n labels the layer. By taking matrix elements of the operator equation $(\omega - \mathcal{H})\mathcal{G}(\omega) = \mathcal{I}$ with the Bloch states, we get the following chain of coupled equations for each $\mathbf{k}_{||}$

$$(\omega - H_{00})G_{00} = \mathbb{1} + H_{01}G_{10} \tag{21}$$
$$(\omega - H_{00})G_{10} = H_{01}^\dagger G_{00} + H_{01}G_{20} \tag{22}$$
$$\vdots$$
$$(\omega - H_{00})G_{n0} = H_{01}^\dagger G_{n-1,0} + H_{01}G_{n+1,0}, \tag{23}$$

where the H_{nm} and G_{nm} are $M \times M$ matrices defined as

$$H_{nm}(\mathbf{k}_{||}) = \langle \Psi_n(\mathbf{k}_{||})|\mathcal{H}|\Psi_m(\mathbf{k}_{||})\rangle, \tag{24}$$
$$G_{nm}(\omega, \mathbf{k}_{||}) = \langle \Psi_n(\mathbf{k}_{||})|\mathcal{G}(\omega)|\Psi_m(\mathbf{k}_{||})\rangle, \tag{25}$$

and we have assumed an ideal surface with $H_{00} = H_{11} = \ldots = H_{nn}$ and $H_{01} = H_{12} = \ldots = H_{n-1,n}$. Note that $n = 0$ corresponds to the surface principal layer. Hence, $G_{00}(\omega, \mathbf{k}_{||})$ defines the surface Green's function.

The general equation for G_{n0} in Eq. (23) can be rewritten as ($n \geq 1$)

$$G_{n0}(\omega) = (\omega - H_{00})^{-1}(H_{01}^\dagger G_{n-1,0} + H_{01}G_{n+1,0}). \tag{26}$$

If we put $n = 1$ in this equation and plug it into Eq. (21) we get

$$[\omega - H_{00} - H_{01}(\omega - H_{00})^{-1}H_{01}^\dagger]G_{00} = \mathbb{1} + H_{01}(\omega - H_{00})^{-1}H_{01}G_{20}. \tag{27}$$

Similarly, we can replace $G_{n-1,0}$ and $G_{n+1,0}$ in Eq. (23) by replacing $n \to n-1$ and $n \to n+1$, respectively. The ensuing equations can be written more compactly as ($n \geq 2$)

$$(\omega - \epsilon_{1s})G_{00} = \mathbb{1} + \alpha_1 G_{20} \tag{28}$$
$$(\omega - \epsilon_1)G_{n0} = \beta_1 G_{n-2,0} + \alpha_1 G_{n+2,0} \tag{29}$$

with

$$\alpha_1 = H_{01}(\omega - H_{00})^{-1}H_{01} \tag{30}$$
$$\beta_1 = H_{01}^\dagger(\omega - H_{00})^{-1}H_{01}^\dagger \tag{31}$$
$$\epsilon_{1s} = H_{00} + H_{01}(\omega - H_{00})^{-1}H_{01}^\dagger \tag{32}$$
$$\epsilon_1 = H_{00} + H_{01}(\omega - H_{00})^{-1}H_{01}^\dagger + H_{01}^\dagger(\omega - H_{00})^{-1}H_{01}. \tag{33}$$

These equations only involve next-nearest-neighbor Green's functions, whereas nearest neighbors have disappeared completely.

Let us now consider the subset of equations formed by taking only even values for n, namely

$$(\omega - \epsilon_{1s})G_{00} = \mathbb{1} + \alpha_1 G_{20} \tag{34}$$
$$(\omega - \epsilon_1)G_{20} = \beta_1 G_{00} + \alpha_1 G_{40} \tag{35}$$
$$\vdots$$
$$(\omega - \epsilon_1)G_{2n,0} = \beta_1 G_{2(n-1),0} + \alpha_1 G_{2(n+1),0}. \tag{36}$$

This set of equations is isomorphic to Eqs. (21)–(23) except for the different zeroth-order matrix elements, $\epsilon_{1s} \neq \epsilon_1$. Thus, we can reiterate the same steps to obtain α_2, β_2, ϵ_2 and ϵ_{2s}. Starting with $\epsilon_0 = \epsilon_{0s} = H_{00}$, $\alpha_0 = H_{01}$ and $\beta_0 = H_{01}^\dagger$, this defines an iterative sequence in which after the i-th step the system of equations reads

$$(\omega - \epsilon_{is})G_{00} = \mathbb{1} + \alpha_i G_{2^i,0} \tag{37}$$
$$(\omega - \epsilon_i)G_{2^i,0} = \beta_i G_{00} + \alpha_1 G_{2^{i+1},0} \tag{38}$$
$$\vdots$$
$$(\omega - \epsilon_i)G_{2^i n,0} = \beta_i G_{2^i(n-1),0} + \alpha_i G_{2^i(n+1),0} \tag{39}$$

with

$$\alpha_i = \alpha_{i-1}(\omega - \epsilon_{i-1})^{-1}\alpha_{i-1} \tag{40}$$
$$\beta_i = \beta_{i-1}(\omega - \epsilon_{i-1})^{-1}\beta_{i-1} \tag{41}$$
$$\epsilon_i = \epsilon_{i-1} + \alpha_{i-1}(\omega - \epsilon_{i-1})^{-1}\beta_{i-1} + \beta_{i-1}(\omega - \epsilon_{i-1})^{-1}\alpha_{i-1} \tag{42}$$
$$\epsilon_{is} = \epsilon_{i-1,s} + \alpha_{i-1}(\omega - \epsilon_{i-1})^{-1}\beta_{i-1}. \tag{43}$$

After the i-th step, this set of equations describes an effective Hamiltonian for a chain with a unit cell enlarged by a factor of 2^i, with nearest-neighbor interactions α_i and β_i, and with zeroth-order Hamiltonian matrix elements ϵ_i and ϵ_{is}. In each layer of this effective chain the effects of nearest-neighbor interactions of all the previous chains are implicitely encoded. Therefore, the norm of the α's and β's typically decreases with i. Once they are small enough, we have $\epsilon_i \simeq \epsilon_{i-1}$ and $\epsilon_{is} \simeq \epsilon_{i-1,s}$. In particular, the RHS of Eq. (37) becomes $\simeq \mathbb{1}$ and we can finally solve for the surface Green's function,

$$G_S \equiv G_{00}(\omega) \simeq (\omega - \epsilon_{is})^{-1}. \tag{44}$$

Thus, we have obtained a good approximation for G_{00}. We remark that the Green's function of the dual (or opposite) surface can be obtained be exchanging the role of α_i and β_i. The Green's function of the bulk is obtained in this process as

$$G_b \equiv \lim_{n\to\infty} G_{nn} \simeq G_{2^i,2^i} \simeq (\omega - \epsilon_i)^{-1}. \tag{45}$$

In practice, one usually wishes to determine the retarded or advanced Green's function. For that, we simply replace in the iterative scheme ω by $\omega \mp i\eta$, with $\eta \in \mathbb{R}$ sufficiently small. Moreover, we note that the great advantage of this scheme is its fast convergence. Typically, one achieves $\beta_i \simeq 0$, $\alpha_i \simeq 0$ to numerical accuracy in fewer than 10 iterations.

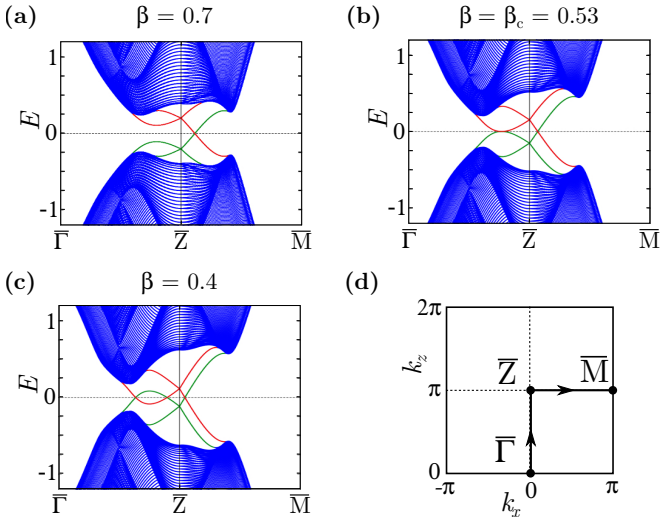

FIG. 6. (color online) Surface energy spectra along high-symmetry lines in the tight-binding model with $a = b = 1$, $t = 1.5$, $\alpha = 0.3$, $d = 0.1$, $\lambda = 0.5$: (a)–(c) energy spectra for different values of the parameter β. Bulk-like states are highlighted in blue, surface states are highlighted in red and green indicating different surfaces. The Fermi energy is at $E_F = 0$ (dashed line). (d) High-symmetry path through the surface BZ corresponding to the displayed energy spectra.

D: Surface energy spectra of the tight-binding model

In Fig. 6, we present energy spectra of the tight-binding model studied in the main text. In particular, Figs. 6(a)–(c) show high-symmetry lines through the k_x-k_z surface BZ which are indicated in Fig. 6(d).

Recall that for $\beta = 0.7$ the surface Fermi surface consists of two Fermi arcs only. They intersect only the $k_z = \pi$ axis in two points that are related by time reversal. The corresponding energy spectrum along $\bar{\Gamma}\bar{Z}$ and $\bar{Z}\bar{M}$ is shown in Fig. 6(a). For the sake of clarity, let us focus on surface states associated with only one of the two surfaces. We see that at $\bar{Z}$ there is an in-gap surface Kramers doublet, relatively far away from the Fermi energy, which is protected by time-reversal symmetry. Away from this point, the doublet is split but the ensuing non-degenerate states evolve differently depending on the considered direction in $\mathbf{k}$ space. Along $\bar{\Gamma}\bar{Z}$ both surface bands terminate at the bulk conduction/valence band. On the contrary, along $\bar{Z}\bar{M}$ one band terminates at the conduction band whereas the other terminates at the valence band. By bulk-boundary correspondence, this behavior is in agreement with the topological invariants of the 2D bulk systems associated with these lines.

By decreasing β, the Kramers doublet at $\bar{Z}$ moves closer to the Fermi energy. At the Lifshitz transition [see Fig. 6(b)], one of the surface bands along $\bar{\Gamma}\bar{Z}$ intersects the Fermi-energy plane tangentially. This is the point where the topology of the Fermi surfaces changes: below a crictical β_c, the Kramers doublet, whose low-energy spectrum is a 2D Dirac cone, is close enough to the Fermi-energy plane to cut out a circular Fermi pocket [see Fig. 6(c)]. To preserve the evenness of the number of crossings, there also has to be a second crossing along $\bar{\Gamma}\bar{Z}$. In contrast, the number of $E = 0$ states along $\bar{Z}\bar{M}$ has not changed. This leads to the formation of new Fermi arcs which intersect only the $k_x = 0$ line of the surface BZ.

Furthermore, we note that the Dirac cone appearing on the surface of the considered Weyl semimetal has a peculiar feature: along one direction, here $\bar{Z}\bar{M}$, it connects the bulk valence to the bulk conduction band, as on the surface of a topological insulator. However, along the perpendicular direction, here $\bar{\Gamma}\bar{Z}$, the Dirac cone is connected to the bulk conduction band (or to the bulk valence band) only. Such a "dangling" Dirac cone can only appear on the surface of a Weyl semimetal where the existence of additional bulk Weyl cones and surface Fermi arcs, to which the Dirac cone is continuously connected in the 2D surface BZ, resolves this apparent contradiction.

[1] P. G. Derry, A. K. Mitchell, and D. E. Logan, Phys. Rev. B **92**, 035126 (2015).
[2] L. Simon, F. Vonau, and D. Aubel, Journal of Physics: Condensed Matter **19**, 355009 (2007).
[3] R. Yu, X. L. Qi, A. Bernevig, Z. Fang, and X. Dai, Phys. Rev. B **84**, 075119 (2011).
[4] L. Fu and C. L. Kane, Phys. Rev. B **74**, 195312 (2006).
[5] M. P. L. Sancho, J. M. L. Sancho, and J. Rubio, Journal of Physics F: Metal Physics **15**, 851 (1985).